Int. J. Heat Mass Transfer. Vol. 36, No. 4, pp. 1049–1060, 1993
Printed in Great Britain

0017-9310/93 $6.00 + 0.00

Structure of air–water bubbly flow in a vertical pipe—I. Liquid mean velocity and turbulence measurements

T. J. LIU† and S. G. BANKOFF
Chemical Engineering Department, Northwestern University, Evanston, IL 60208-3120, U.S.A.

(*Received* 24 *June* 1991 *and in final form* 24 *January* 1992)

Abstract—The liquid-phase turbulent structure of an air–water, bubbly upflow in a circular pipe has been investigated experimentally. Liquid-phase local velocities and turbulent stresses were simultaneously measured, using both one- and two-dimensional hot-film anemometer probes. A highly-accurate digital process method, based on threshold combinations of level and slope, was developed to identify the phases. Systematic measurements were conducted under 48 flow conditions covering a range of local void fraction from 0 to 50%. The important experimental results and parametric trends are summarized and discussed. Finally, the present data are compared with some other data sources and existing models.

INTRODUCTION

TURBULENT bubbly liquid–gas flow occurs in many important technical applications, and hence has been widely studied. However, it is only in recent years that much progress has been made in understanding the local structure of these flows. The pioneering studies of Serizawa *et al.* [1] and of Theofanous and Sullivan [2], in which local measurements of liquid velocities and turbulent intensities in pipe flow, using, respectively, hot-film anemometers and laser-doppler anemometer, provided impetus for further studies. Along with further experimental data, Sato and Sekoguchi [3], Lance and Bataille [4], Marie and Lance [5], Wang [6], Lee [7], Michiyoshi and Serizawa [8], Matsui [9], Serizawa *et al.* [10] and Zun *et al.* [11] provided models of ever-increasing complexity for the steady, local-average bubble size radial distribution, coalescence rates, and bubble-induced liquid turbulence. These take into account one or more of the following: wall–liquid (single-phase), bubble–bubble, bubble–wake, and bubble–liquid interactions. Since none of these can be deduced from first principles for a multi-bubble turbulent array, it is necessary to employ a number of adjustable constants. In attempting to verify these constants, it is found that substantial disagreement exists between data sets taken under apparently similar conditions [12]. From another point of view, considerable progress has been made in recent years in constructing multi-dimensional two-fluid models for bubbly flows, as summarized by Lahey and Lopez de Bertodano [13], but these do not depend upon bubble diameter distributions, either locally or globally. It is clear, however, that information of this nature is needed in order to progress beyond the selection of empirical constants in the time-averaged phasic momentum equations. It was for these reasons that the present experimental work was undertaken. Data were taken with hot-film anemometers and a two-point resistivity probe in systematic fashion over the range J_g: 0.027–0.347 m s^{-1}, and J_f: 0.376–1.391 m s^{-1}. A total of 48 flow conditions were employed, in which local liquid velocity, intensity, and Reynolds stress were measured in fully-developed air–water bubbly upflow in a vertical glass pipe. The bubble diameters were in a narrow range of 2–4 mm. In addition, the local void fraction, bubble frequency, bubble velocity and bubble size distribution were measured, all as a function of radial position. Rigorous standards of reproducibility and accuracy were maintained. It is hoped that this data set will serve as a standard against which models can be tested, at least over the range of conditions employed herein. In addition, some comparisons are made with the previous work. Because of space limitations, only some of the liquid-phase data are presented herein, and the gas-phase data in a companion paper [14]. Complete data can be obtained from Liu [15], or by writing to the first author.

EXPERIMENTAL FACILITY

A schematic diagram of the experimental system is shown in Fig. 1. The test section was a 2800 mm long, vertical smooth acrylic tubing, with inside diameter of 38 mm, which was made up of two major spool pieces. The lower piece was a probe measuring section, while the upper piece was a hold-up section. A transparent, water-filled, rectangular box was fitted onto the test section, to allow undistorted photographic measurements of the bubble size.

† Present address: Institute for Nuclear Energy Research, P.O. Box 3-3 Lung Tan, Taiwan 32500, Republic of China.

NOMENCLATURE

A	cross-sectional area [m^2]
D	diameter of pipe [m]
g	gravitational constant [m s^{-2}]
J_f, J_g	superficial velocities of liquid and gas flow [m s^{-1}]
K	tangential cooling factor
L	entrance length [m]
R	radius of pipe [m]
r	coordinate in radial direction [m]
(U, V)	instantaneous local velocity in axial and lateral directions [m s^{-1}]
(u, v)	instantaneous local velocity fluctuation in axial and lateral directions [m s^{-1}]
(u_f, v_f)	root-mean-square values of u and v [m s^{-1}]
U^*	local friction velocity [m s^{-1}]
U_b	local bubble velocity [m s^{-1}]
U_f	local liquid phase velocity [m s^{-1}]
U_0	velocity at pipe center [m s^{-1}].

Greek symbols

α	local void fraction
$\bar{\kappa}$	time-average value of κ
$\langle\kappa\rangle$	cross-sectional area-average value of κ
$\tilde{\kappa}$	root-mean-square value of κ
ρ	density [kg m^{-3}]
τ_w	wall shear stress
τ	local shear stress
θ	yaw angle [deg].

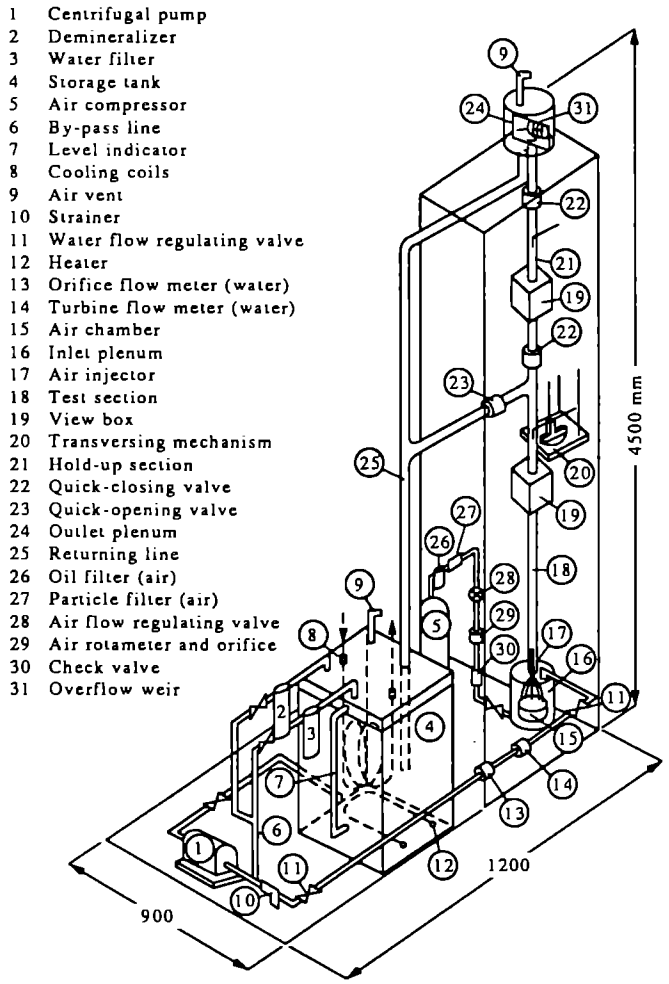

FIG. 1. Three-dimensional schematic of testing loop.

The distilled water was circulated from a storage tank through the metering section by a centrifugal pump. The storage tank contained cooling coils and heater in order to control closely the flow temperature to 10 ± 0.01°C at the measuring station ($L/D = 36$) during the entire course of all experiments. This close temperature control was a key point in minimizing the temperature drift of the hot-film sensors. The gas and liquid flows were measured by well-calibrated orifice flowmeters, and indicated by manometers. The air flow entered the air chamber at the lower part of the inlet plenum. Bubbles were produced by injecting air into a bundle of 64 equally-spaced, 0.1 mm hypodermic needles at the upper part of the inlet plenum. This bubble generating method proved to have the advantages of: (1) minimizing bubble coalescence, resulting in a uniform bubble size distribution when the bubbles detached from the injector; and (2) generating small bubbles (2–4 mm equivalent diameter) at the measuring station. A schematic diagram of the inlet plenum and bubble generator is shown in Fig. 2. Two-phase bubbly flow was realized by mixing the air bubbles uniformly with the water stream at the entrance of the test channel. The two-phase mixture was separated in the outlet plenum. Water was then returned to the storage tank to be recirculated, while air was vented to the atmosphere. Loop water was periodically recirculated through the demineralizer and filters to maintain the specific resistivity of the circulating water above $2 \times 10^6\ \Omega\ \text{cm}^{-1}$.

The local position of the probe travelling along the radial direction of the test section was accurately controlled by the probe transversing mechanism. It consisted of a micrometer screw on which the probe support was fastened. The support could be rotated freely in a plane parallel to the water flow. Thus the hot-film sensor might be adjusted to various yaw angles as read from a protractor during calibration. With the aid of a close-up lens, the uncertainty of the probe position could be controlled within 0.05 mm.

In order to optimize the signal resolution and thus increase the data accuracy, the analog output of the anemometer (TSI-150) was filtered, gained and suppressed by a signal conditioner (TSI-157). Then the signal was sampled by a TSI IFA-200 multichannel digitizer, with sampling rate up to 500 kHz. Following digitization, status data were sent to the computer and stored for later analysis.

MEASURING METHODOLOGY

One-dimensional measurement

For these measurements, the TSI 1218-20W boundary layer hot-film sensor (0.05 mm o.d. × 1 mm) was placed normal to the flow stream, with the x-direction coinciding with the axial direction of the test section ($\theta = 0°$). A nonlinear calibration relation could thus be used of effective cooling velocity (U_{eff}) versus anemometer voltage output (E_a) to interpret the local mean velocity (U_f) and the axial turbulent fluctuation (u_f) as

$$U_f = \overline{U_{\text{eff}}}(0°) \tag{1}$$

$$u_f = \sqrt{(\overline{u^2})} = [\overline{U_{\text{eff}}^2}(0°) - \overline{U_{\text{eff}}}(0°)^2]^{1/2}. \tag{2}$$

Two-dimensional measurement

In this case, TSI 1246-60 W dual-sensor X-type hot-film probe (0.15 mm o.d. × 2 mm long) was used to measure the liquid velocity, U_f, axial and lateral turbulence (u_f, v_f), and Reynolds stress ($-\rho\overline{uv}$). Consider a two-dimensional probe, with (U, V) being the axial and radial velocities, respectively, making angles $\theta + \pi/2$ and θ with the pipe axis for sensor-1 and sensor-2, respectively. One can write the velocity components in terms of an effective cooling velocity for each sensor

$$U_{\text{eff},1} = \{(U\cos\theta - V\sin\theta)^2 + K_1^2(U\sin\theta + V\cos\theta)^2\}^{1/2} \tag{3a}$$

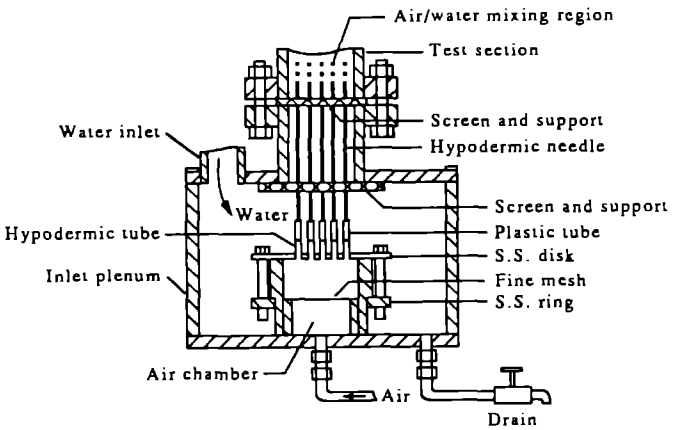

FIG. 2. Test section inlet plenum and bubble generator.

$$U_{\text{eff},2} = \{(U\sin\theta + V\cos\theta)^2 + K_2^2(U\cos\theta - V\sin\theta)^2\}^{1/2} \quad (3b)$$

where suffix 1 and 2 refer to sensor-1 and -2, respectively. The tangential cooling factor (K) is obtained from yaw angle sensitivity calibration. With further analysis [15] one can get the effective fluctuating terms, which can be expressed as a linear system as

$$\mathbf{u}_{\text{eff}} = \mathbf{A}\mathbf{X} \quad (4)$$

where

$$\mathbf{u}_{\text{eff}} = \begin{bmatrix} \overline{u_{\text{eff},1}^2} \\ \overline{u_{\text{eff},2}^2} \\ \overline{u_{\text{eff},1}u_{\text{eff},2}} \end{bmatrix}, \quad \mathbf{X} = \begin{bmatrix} \overline{u^2} \\ \overline{v^2} \\ \overline{uv} \end{bmatrix},$$

$$\mathbf{A} = \begin{bmatrix} a_1^2 & b_1^2 & 2a_1b_1 \\ a_2^2 & b_2^2 & 2a_2b_2 \\ a_1a_2 & b_1b_2 & a_1b_2 + a_2b_1 \end{bmatrix}$$

$$a_1 = \sqrt{a}, \quad a_2 = \sqrt{r}, \quad b_1 = c_1/2\sqrt{a}, \quad b_2 = t/2\sqrt{r},$$

$$c_1 = b/2\sqrt{a} - c^2/8a^{3/2}, \quad c_2 = s/2\sqrt{r} - t^2/8r^{3/2},$$

$$a = \cos^2\theta + K_1^2\sin^2\theta, \quad r = K_2^2\cos^2\theta + \sin^2\theta,$$

$$b = \sin^2\theta + K_1^2\cos^2\theta, \quad s = K_2^2\sin^2\theta + \cos^2\theta,$$

$$c = -2(1-K_1^2)\sin\theta\cos\theta,$$

$$t = 2(1-K_2^2)\sin\theta\cos\theta.$$

Thus, all three two-dimensional time averaged fluctuating components can be determined from equation (4).

In this study, we also use the expression for the single-inclined hot-wire effective cooling velocity, derived by Champagne and Sleicher [16] to deduce a closed form for the three two-dimensional turbulent stress components as

$$\overline{u^2} = (\overline{u_{\text{eff},1} + u_{\text{eff},2}})^2/(2B_1) \quad (5a)$$

$$\overline{v^2} = (\overline{u_{\text{eff},1} - u_{\text{eff},2}})^2/(2B_2) \quad (5b)$$

$$\overline{uv} = (\overline{u_{\text{eff},1}^2} - \overline{u_{\text{eff},2}^2})/(2B_1B_2) \quad (5c)$$

where

$$B_1 = 1 + (1/2)K^2 - (1/8)K^4,$$

$$B_2 = 1 - (3/2)K^2 + (7/8)K^4.$$

Both equations (4) and (5) were used to deduce the test data in the present study. The results were very consistent, as shown by reproducibility within 0.2%.

PHASE DISCRIMINATION AND DATA PROCESSING

When hot-film anemometry, as well as other techniques, is used to study two-phase flow, the first important problem is to identify the phases. In order to solve this problem, the hot-film anemometer response to the presence of a liquid–bubble interface must be studied. Figure 3 is the typical hot-film anemometer response, measured with a digitized sampling rate of 5 kHz. It is clear that the bubble was detected in time period from A to D. D to E was a detachment tail, due to rewetting of the film sensor, and did not represent a correct liquid signal. Therefore, the detected signal ABCDE should be processed before evaluating liquid turbulence quantities. Before the formal test program, an extensive study was made to examine a number of published phase discrimination methods by checking the digitized signal. The results showed that it is difficult completely to handle the complex phase identification by using only a simple level threshold or derivative algorithm.

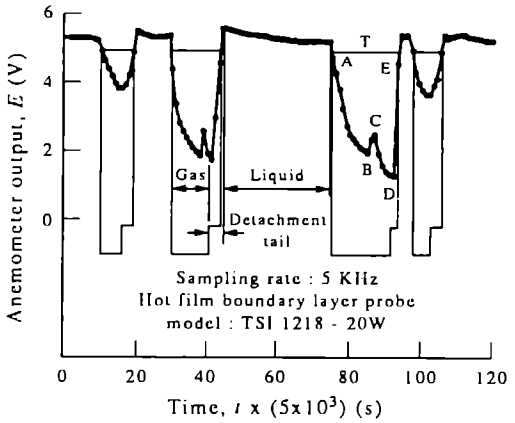

FIG. 3. Typical digitized sampling raw data and phase discrimination result.

A new phase discrimination method was therefore developed in this study. Eight simple algorithms covering normal and closely-spaced bubble–probe interactions were proposed. In each algorithm, the phase was identified based on a combination of the level and slope threshold. Before discussing the details of each algorithm some parameters should be defined as follows:

T = level threshold, S = slope threshold,

R_i = ith data sample,

$P_b = R_i - R_{i-1}$ (backward slope),

$P_f = R_i - R_{i+1}$ (forward slope),

$R_b = |P_b|$, $R_f = |P_f|$

(magnitude of P_b and P_f).

If $R_i > T$, and if any of the following eight conditions is satisfied, then the current R_i is in the liquid phase and is stored for later processing. Otherwise, the current R_i is in the gas phase and should be eliminated. The eight algorithms are listed as follows:

Case (a). If at least two liquid data points lie between two consecutive bubbles

(1) $R_h < S$ and $R_l < S$ (remain in liquid)

(2) $R_h < S$ and $P_l > S$ (entering bubble)

(3) $R_{i+1} > T$ and $P_h > S$ and $R_l < S$ (entering liquid).

If there is overshooting due to bubble approaching

(4) $P_l < 0$ and $R_h < S$ and $R_l < 1.5S$ and $R_{i+2} < R_{i+1}$ and $|R_{i+2} - R_{i+1}| > S$.

If there is overshooting due to bubble detaching

(5) R_{i-1} in gas and $R_{i+1} > T$ and $P_l > 0$ and $P_h > S$ and $R_l < 1.5S$.

Case (b). If only one liquid data point lies between two consecutive bubbles

(6) $P_h > 2S$ and $P_l > S$

(7) $P_h > S$ and $P_l > 2S$

(8) $R_{i-1} < T$ and $R_{i+1} < T$.

The main function of algorithms (6)–(8) is to identify the bubble number. The slope threshold, S, is simply a scale in terms of two consecutive samples of voltage difference. For a fixed sampling rate, S is set to a constant satisfying all of the flow conditions. Therefore, before processing the data only the level threshold value T should be set. It is well known that for different flow conditions the anemometer will respond with a different level of liquid voltage signal. Although the level threshold, T, depends on the flow conditions, the advantage of this phase discrimination method is that it is not necessary to restrict the setting to a value very close to the liquid signal, due to the help of the slope thresholds combination (S, P_h, P_l, R_h, R_l) algorithms. In the actual case, to preset an accuracy level threshold is very difficult. However, it is one of the important requirements in most of the existing phase discrimination method found in the literature.

After checking the digitized and labelled phase discrimination results in all test conditions, the above-mentioned algorithms were found successfully to handle this task. Typical phase discrimination results are also shown in Fig. 3. For a better resolution of the turbulent fluctuation and higher accuracy in phase discrimination, a 5 kHz sampling rate with 12 s sampling time was selected. In addition, the mean flow itself varies on a time scale much longer than the turbulent fluctuations. The sampling time must be smaller than the period of the unsteadiness in the mean flow. In this study, at each local measuring point, the data were collected and averaged over six blocks. Each data block with a sampling time of 2 s was analyzed separately to ensure statistically stationary results.

RESULTS AND DISCUSSION

Single-phase measurements and comparison

Before beginning the two-phase measurements, single-phase liquid measurements were made in the same equipment to calibrate the instrumentation, verify their consistency with known results, and to serve as a reference for later comparison with two-phase measurements. The local velocity, turbulent fluctuations in the axial and lateral directions, as well as the Reynolds stress distribution, at $L/D = 36$ for different superficial liquid velocities are shown in Fig. 4(a). A linear increase in the three stress components is observed. The rapid increase of the axial fluctuation when the probe is close to the wall may be due to wall-induced turbulence. The axial turbulence fluctuations near the wall and up to $r/R = 0.997$ were measured by a boundary layer probe. Even at this close proximity to the wall, u_l does not decrease. This implies that there exists a very thin viscous sublayer near the wall which the boundary-layer probe does not reach. This phenomenon is confirmed from Laufer's data [17] in channel flow at $Re = 38\,000$. The maximum axial turbulence fluctuation occurs when the wall is very close, with $r/R = 0.9983$. The measured velocity profiles and turbulent stresses also are non-dimensionalized with respect to the characteristic velocities U_0 and U^*, respectively, in order to be compared with Laufer's data [18] at $Re = 50\,000$. As presented in Fig. 4(b), the results are in good agreement.

Two-phase water velocity profiles

Figure 5 shows the water velocity profiles at constant liquid flow and at constant gas flow rates. The introduction of gas at a low flow rate into a water flow generally flattens the velocity profile, with a relatively steep decrease close to the wall. This phenomenon is especially pronounced at high water flow rates. The local water velocity near the pipe core region is sometimes lower than in single-phase water flow, such as in the low-quality bubbly flow regime at high water flow rates. For low liquid flows, the velocity profile changes from flat at low gas flow to convex at high gas flow. For high liquid flows the opposite tendency was observed.

The integrated local water velocity (U_l) measurements were compared with the superficial water velocity (J_l), which was directly measured by the calibrated orifice. From the locally-measured α and U_l, we can calculate the area-averaged volume flux defined by

$$\langle J_l \rangle = \frac{1}{A} \int_A (1-\alpha) U_l \, dA \qquad (6)$$

where α is the local void fraction measured from the resistivity probe [14]. The total of 48 flow conditions were checked, and the uncertainty is presented in Fig. 6. The uncertainty for every flow condition is within $\pm 5\%$. Most of the data for liquid-phase parameters were checked more than twice. The consistency of

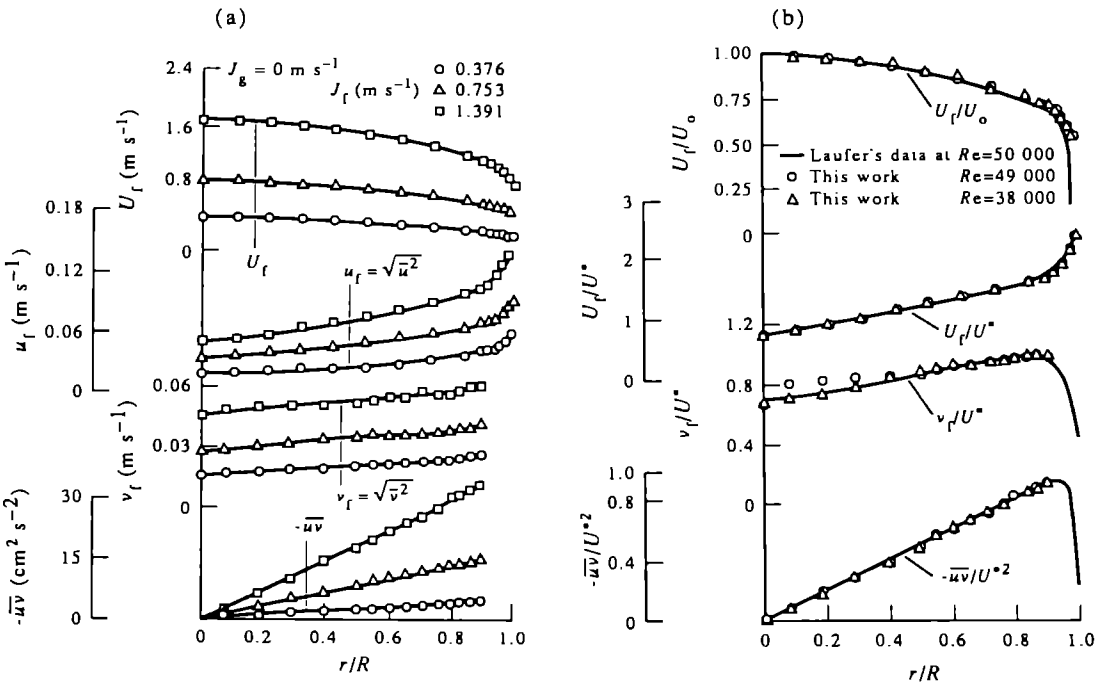

FIG. 4. Single-phase measurements (a) and comparison with Laufer's data [17, 18] (b).

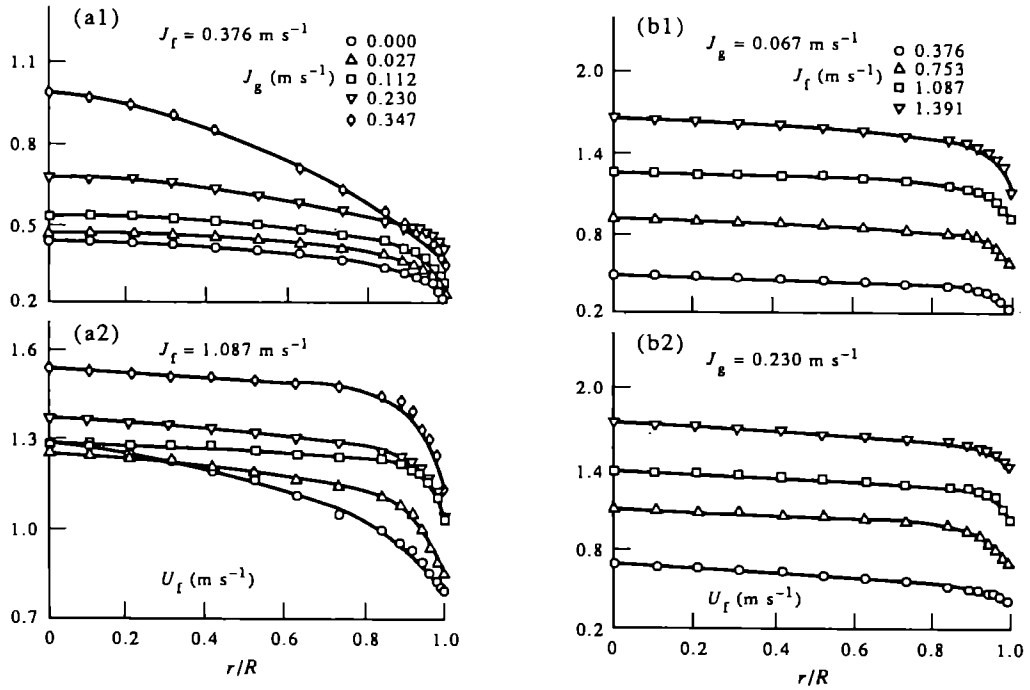

FIG. 5. Liquid-phase velocity distributions: (a) at constant J_f; (b) at constant J_g.

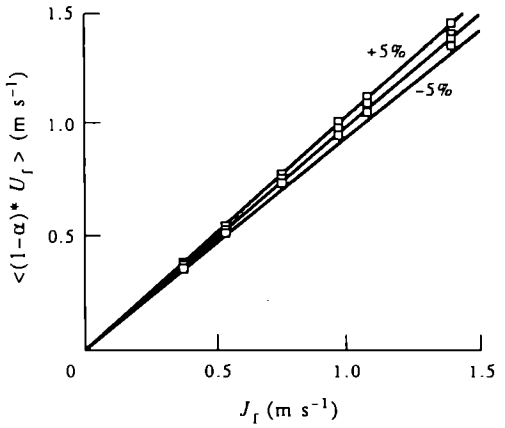

FIG. 6. Uncertainty estimation.

liquid velocity was within ±1.5%, and the turbulent stresses were within ±3%.

Turbulent stress profiles

The profiles of both the axial turbulent fluctuation (u_f) and the intensity (u_f/U_f) with increasing void at constant liquid flow and of increasing liquid flow at constant gas flow are shown in Figs. 7 and 8. Axial turbulent fluctuations generally increased toward the wall and became flat at the core region. However, as the liquid flow decreased, the concave profile generally became flat near the wall, and finally became convex at low flow conditions. The axial turbulence at low liquid flow and high gas flow conditions decreased near the wall. The turbulence increased strongly upon increasing the gas flow, especially at low liquid flow in the pipe core region. This effect of bubble agitation becoming dominant at a low liquid flow rate was also confirmed by Sato and Sadatomi [19] from the evaluation of their bubble eddy diffusivity data. This enhanced turbulence might be related to the observed trend that the bubble-induced turbulence is more pronounced in the core region at low flow conditions.

The effect of increasing water flow at constant gas flow was to decrease the liquid velocity fluctuation. This effect was observed over most of the cross-sectional area, except in the region near the wall where the reverse tendency was observed. This interesting phenomenon near the wall was found at all constant gas flow conditions. The profiles of corresponding axial turbulent intensity, u_f/U_f, were obtained. Axial turbulent intensity generally increased toward the wall and became flat in the core region. The increased gas flow had the same tendency as the absolute turbulence u_f to augment u_f/U_f. However, increasing liquid flow at constant gas flow decreased the turbulent intensity, both at the pipe center and at the wall. Thus, the liquid-phase turbulence is relatively damped by increasing the water flow, even though the absolute turbulence level increases near the wall.

The experimental results also imply that introducing bubbles into the liquid flow enhances the lateral momentum transfer, and promotes a relatively uniform turbulence distribution in the core region. Although data cannot be taken close to the wall with the X-probe, an interesting tendency similar to the axial turbulence still can be observed, except at a lower turbulence level compared with the axial component.

In turbulent flow, the Reynolds stress, $-\rho\overline{uv}$, acting on the local circumferential surface was virtually equal to the total shear stress everywhere in the pipe, except near the wall, where a laminar viscous shear layer existed. This Reynolds stress plays a dominant role in the process of mean momentum transport by turbulent motion. The single-phase Reynolds stress always increased linearly with distance from the pipe center, while the profiles of two-phase Reynolds stress increased nearly linearly in the core region, and then sharply increased close to the wall. This wall effect was especially pronounced at low liquid flow and high void fraction conditions. The experimental evidence also indicates that the Reynolds stress becomes larger, either by increasing the gas flow at constant liquid flow, or by increasing the liquid flow at constant gas flow, especially close to the wall.

It is interesting to note that the radial profiles of the relative Reynolds stress showed the same tendency as the relative axial and lateral turbulence on the effect of increasing gas flow and liquid flow. The consistent tendency of these relative turbulent stresses strongly implies that the local turbulent motion is directly related to the local main stream motion in the two-phase bubbly flow.

Because the bubbles in turbulent two-phase flow enhance both dissipation and production of turbulence kinetic energy, the presence of bubbles sometimes suppresses the level of turbulence, making it lower than the corresponding single-phase flow turbulence. This turbulence suppression phenomenon was found at high liquid flow and low void fraction conditions for both the axial (u_f) and lateral (v_f) directions, as well as for the turbulent shear stress ($-\rho\overline{uv}$).

Bubble-induced turbulence

One simple measure of the bubble-induced turbulence (u'', v'') components is the difference between the two-phase bubbly flow turbulence (u, v) and the corresponding single-phase wall-generated (u', v') components, as suggested by Sato and Sadatomi [19]. However, as discussed above, the presence of bubbles can reduce the two-phase velocity fluctuations compared to the single-phase velocity fluctuations at the same J_f. The net contribution will be positive when the production of turbulent kinetic energy by the bubbles outweighs the dissipation by the bubbles. Based on this superposition hypothesis, the enhanced two-phase fluctuations u and v can be expressed as

$$u = u' + u'', \quad v = v' + v'' \tag{7}$$

and then

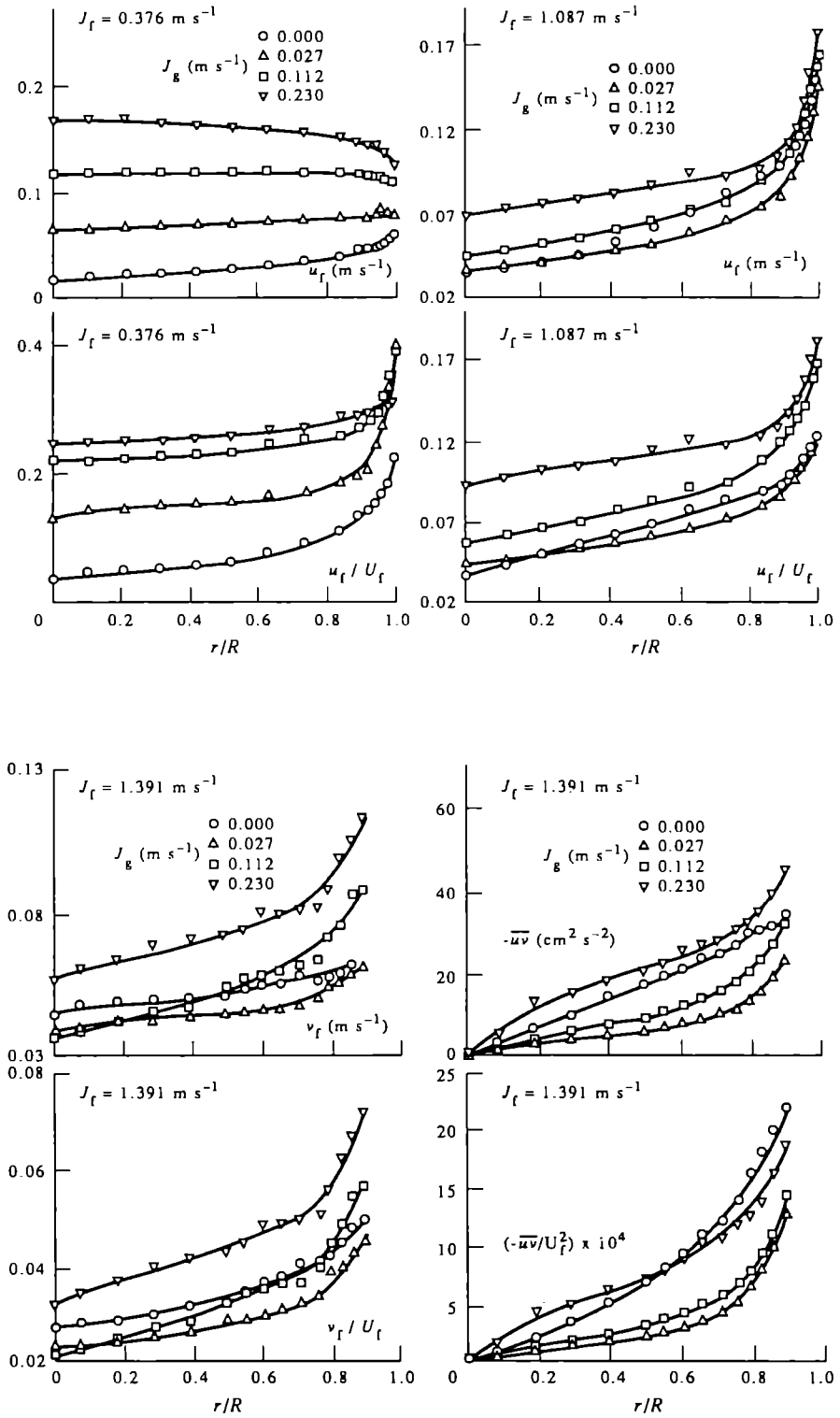

FIG. 7. Liquid-phase turbulent fluctuation and intensity at constant J_f.

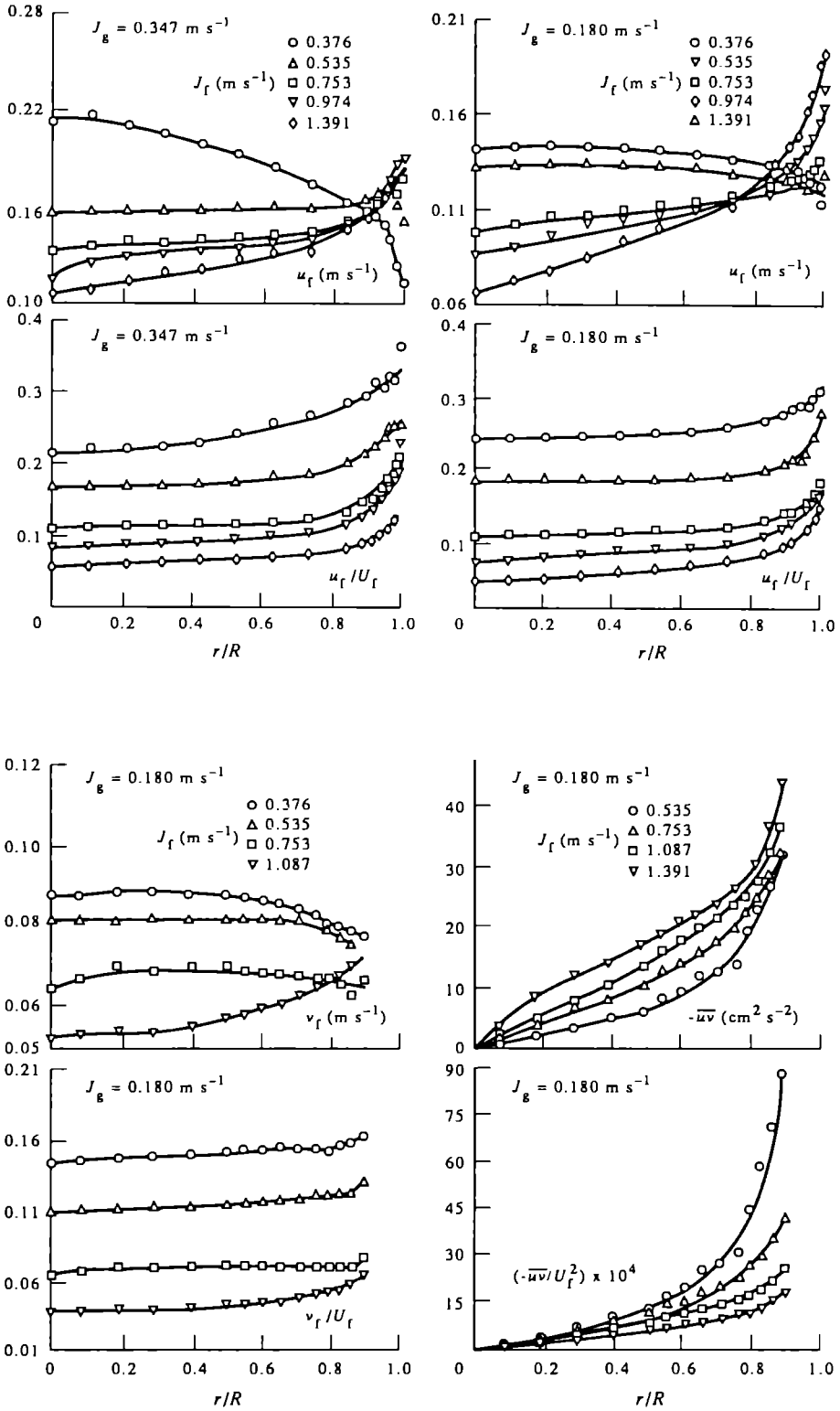

FIG. 8. Liquid-phase turbulent fluctuation and intensity at constant J_g.

$$(u_f)^2 = (\sqrt{(\overline{u^2})})^2 = (\widetilde{u'})^2 + (\widetilde{u''})^2,$$
$$(v_f)^2 = (\sqrt{(\overline{v^2})})^2 = (\widetilde{v'})^2 + (\widetilde{v''})^2. \quad (8)$$

The bubble-induced turbulence in the axial ($\widetilde{u''}$) and lateral ($\widetilde{v''}$) directions can be calculated from the measured data of single-phase ($\widetilde{u'}$, $\widetilde{v'}$) and two-phase (u_f, v_f). The calculated radial profiles of bubble-induced turbulence $(\widetilde{u''}/u_f)^2$ and $(\widetilde{v''}/v_f)^2$ (Fig. 9), indicate that the energy ratio of bubble-induced turbulence to the total turbulence strongly depends on the flow conditions. Generally, this ratio increased with increasing gas flow. However, increasing the liquid flow at constant gas flow rate led to decreased energy ratio. These observed trends were consistent with the trends of relative turbulence discussed above. The results also indicated that most of the local turbulent energy at the pipe center contributed by the bubble agitation would be reduced close to the wall. It was observed that at the lowest liquid flow ($J_f = 0.376$ m s^{-1}), the bubble-induced turbulence contributes more than 90% of the total energy in most of the core region. This generally decreasing trend near the pipe wall does not reflect the wall peaking void fraction effect observed under the same flow conditions [14].

The axial bubble-induced turbulence $\widetilde{u''}$ is plotted against local void fraction in Fig. 10. In this figure, two different void fraction-dependency models to predict $\widetilde{u''}$ proposed by Michiyoshi and Serizawa [8] are also included. Most of the data plotted by these authors fall close to curve B, whereas most of the data measured in this study are closer to curve A. The reason for this discrepancy is not clear.

COMPARISON BETWEEN EXPERIMENTS AND MODELS

The centerline turbulence measured in this study was compared with the Theofanous and Sullivan [2] model. The bubble-induced turbulence $\widetilde{u''}$ was also calculated. The results presented in Fig. 11 show fairly good agreement.

The present experimental data are compared with the data of Serizawa *et al.* [20] and Wang [6], under similar flow conditions. The test section inside diameter was 60 mm in the Serizawa experiment, 57 mm

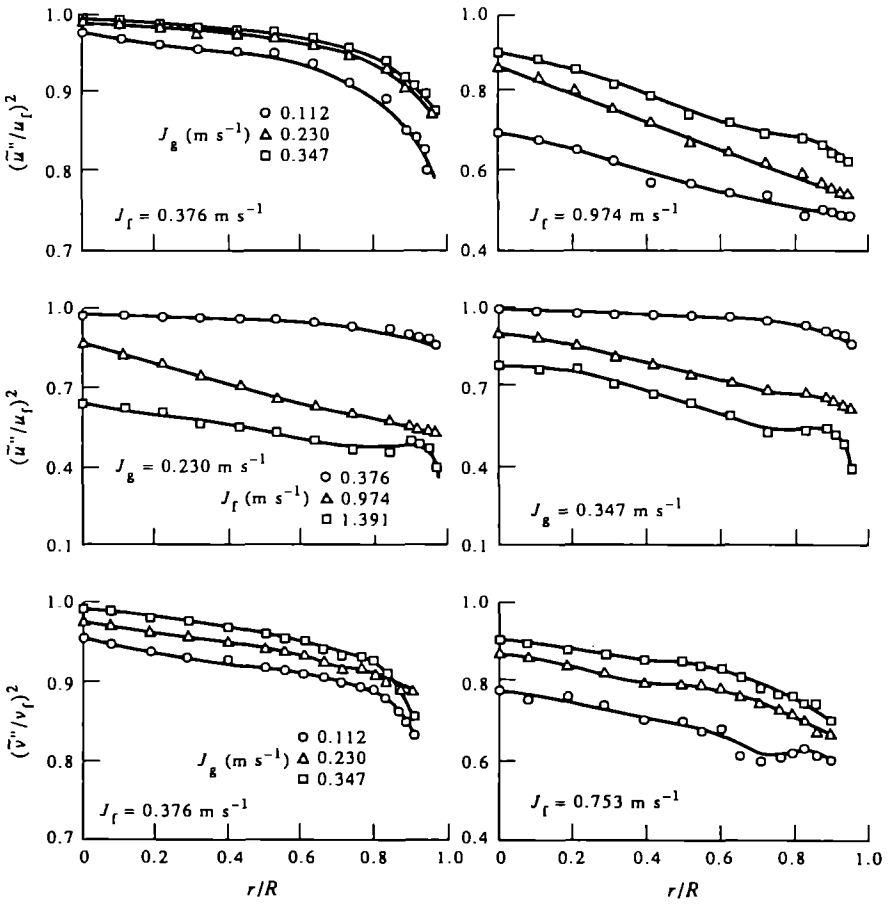

FIG. 9. Radial variation of bubble-induced turbulence.

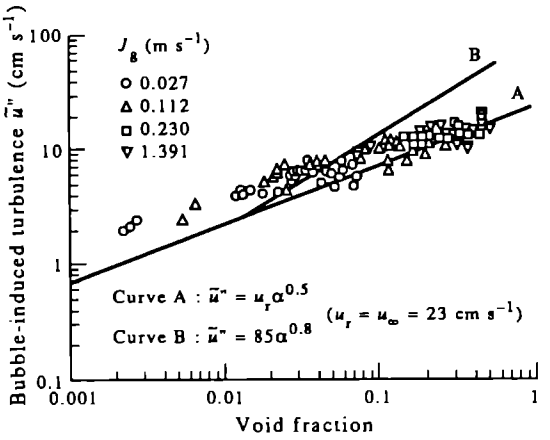

FIG. 10. Bubble-induced turbulence vs void fraction.

in the Wang experiment, and 38 mm in the present study. The profiles of liquid-phase velocity and its turbulence as well as the void fraction distribution are compared in Fig. 11. Although the curves are generally in fairly good agreement, there are differences, possibly due to differences in entrance geometry and bubble injection method, causing different sizes and initial distributions of bubbles, and also the different tube diameters. Since different bubble size distributions may result in different flow regimes even at the same flow condition, they clearly affect the local turbulent structure. The lift force on an individual bubble depends on the bubble diameter, and probably also the wall–bubble interaction force, although this is not as well understood.

The liquid–velocity data were also compared with the effective eddy diffusivity superposition model proposed by Sato and Sadatomi [19]. By following their backward-difference iterative scheme, and adjusting the wall shear stress, a predicted velocity profile was obtained with a relative error between the integrated velocity profile and the measured mass flow rate less than 0.2%. A comparison was made (not shown) of the liquid velocity distributions predicted by the theory with those obtained experimentally, coupled with the measured void fraction distributions. It was found that the predictions are generally in agreement with the experiments of Serizawa and the present data under high flow conditions, but not under low flow conditions.

It is interesting to note that the predicted liquid velocity profiles are in fairly good agreement with measurements close to the wall, but underpredict the centerline velocity. These trends seem unreasonable in the real situation. It is well known that a more reliable calibration curve of the hot-film probe can be obtained by performing the calibration at the pipe centerline than at any other radial position, owing to the axisymmetry of the fully-developed flow. In order to ensure that the velocity data exhibit negligible calibration drift, the centerline velocity often becomes an important check point for the initial and final local measurements in a run. It is thus reasonable to have the smallest uncertainty for the center velocity, as well as the core velocities. Relatively large uncertainty may occur near the wall because of the higher turbulence resulting from the interaction of the wall and the concentrated bubble layer close to the wall. In order to minimize the above-mentioned deleterious effect, an alternative approach using a forward-difference iterative scheme with the starting point at the center was tried. This allows the data with the least estimated relative error to be used as the initial condition. As expected, the corresponding predicted results were found to have a significant improvement in the core region, with a relatively small deviation near the wall. This forward-difference approach thus gives better agreement with the real physics, and reduces the gross error of the prediction.

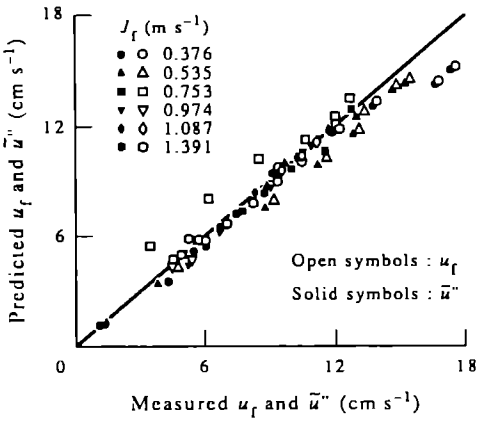

FIG. 11. Comparison of Theofanous and Sullivan correlation with present data.

CONCLUDING REMARKS

(1) An extensive study of the liquid-phase turbulent structure of air–water bubbly flow has been made, using both one- and two-dimensional hot-film probes, under 48 well-defined flow conditions. Great care was taken to keep the estimated errors as low as practicable, so that the data base should be useful for model formulation and for code validation. Gas-phase measurements under the same flow conditions are given in a companion paper.

(2) An improved digital processing method, based on threshold combinations of level and slope, was developed to identify the phases with the hot-film anemometer. The method has the advantage of incorporating more of the real physics of bubble–probe interaction than previous slope-threshold algorithms.

A definitive comparison cannot be made, however, since both methods depend on integrating the radial void fraction profile and comparing with the mean density measurements for calibration and checking.

(3) Increasing the gas flow rate at constant liquid flow rate increases not only the absolute turbulence, but also all the turbulent intensities, u_f/U_f, v_f/U_f, and $-\rho\overline{uv}/U_f^2$. However, increasing the liquid flow at constant gas flow rate reduces the liquid phase turbulence in the core region, but increases the turbulence in the wall region. This also results in decreased turbulent intensities over the whole cross-section. The same trends are exhibited by the bubble-induced turbulent intensity, showing the strong interaction between the bubbles and the liquid velocity field.

(4) The present liquid velocity profile data are compared with those of Serizawa *et al.* and of Wang under fairly similar flow conditions, and with the model of Sato and Sadatomi for prediction of liquid–velocity profiles. There is reasonable agreement with the Serizawa data under high flow conditions, but not at low flow conditions. The reasons for the disagreement may be associated with the bubble generation method or the different mean bubble diameter/tube diameter ratio. A forward-difference integration was used for velocity profile results, and showed fairly good agreement between predictions and experiments for all three data sources. The centerline turbulence data were also compared with the Theofanous and Sullivan model. The results were in fairly good agreement.

REFERENCES

1. A. Serizawa, I. Kataoka and I. Michiyoshi, Turbulence structure of air–water bubble flow, *Int. J. Multiphase Flow* **1**, 221–246 (1975).
2. T. G. Theofanous and J. Sullivan, Turbulence in two-phase flows, *J. Fluid Mech.* **116**, 343–362 (1982).
3. Y. Sato and K. Sekoguchi, Liquid velocity distribution in two-phase bubbly flow, *Int. J. Multiphase Flow* **2**, 79–95 (1975).
4. M. Lance and J. Bataille, Turbulence in the liquid phase of a bubbly air–water flow. In *Advances in Two-phase Flow and Heat Transfer*, Vol. 1 (1983).
5. J. L. Marie and M. Lance, Turbulence measurements in two-phase bubbly flows using laser doppler anemometry. In *Measuring Techniques in Gas Liquid Two-phase Flows, IUTAM Symp.*, Nancy, France (1984).
6. S. K. Wang, 3-D turbulence structure measurements in air/water two-phase flows, Ph.D. Thesis, Rensselaer Polytechnic Institute (1986).
7. S. J. Lee, Turbulence modeling in bubbly two-phase flows, Ph.D. Thesis, Rensselaer Polytechnic Institute (1986).
8. I. Michiyoshi and A. Serizawa, Turbulence in two-phase bubbly flow, *Nucl. Engng Des.* **95**, 253–267 (1986).
9. G. Matsui, Characteristic structure of upward bubble flow under the same flow conditions, *Proc. Japan–U.S. Seminar on Two-phase Flow Dynamics*, Ohtsu, Japan, paper E.2 (1988).
10. A. Serizawa, I. Kataoka, I. Zun and I. Michiyoshi, Bubble size effect on phase distribution, *Proc. Japan–U.S. Seminar on Two-phase Flow Dynamics*, Ohtsu, Japan, paper 3.3 (1988).
11. I. Zun, I. Kljenak and A. Serizawa, Bubble coalescence and transition from wall void peaking to core void peaking in turbulent bubbly flow, *Proc. Japan–U.S. Seminar on Two-phase Flow Dynamics*, Ohtsu, Japan, paper C.3 (1988).
12. A. Serizawa and I. Kataoka, Phase distribution in two-phase flow, *ICHMT Int. Seminar on Transient Phenomena in Multiphase Flow*, Dubrovnik, Yugoslavia (1988).
13. R. T. Lahey, Jr. and M. Lopez de Bertodano, The prediction of phase distribution using two-fluid models. In *ASME/JSME Thermal Engng Proc.*, Reno, Nevada, Vol. 2, pp. 193–200 (1991).
14. T. J. Liu and S. G. Bankoff, Structure of air–water bubbly flow in a vertical pipe—II. Void fraction, bubble velocity and bubble size distributions, *Int. J. Heat Mass Transfer* **36**, 1061–1072 (1993).
15. T. J. Liu, Experimental investigation of turbulence structure in two-phase bubbly flow, Ph.D. Thesis, Northwestern University (1989).
16. F. H. Champagne and C. A. Sleicher, Turbulence measurements with inclined hot wires, part 2: hot-wire response equations, *J. Fluid Mech.* **28**, 177–182 (1967).
17. J. Laufer, Investigation of turbulent flow in a two-dimensional channel, NACA report 1053 (1953).
18. J. Laufer, The structure of turbulence in fully developed pipe flow, NACA report 1174 (1954).
19. Y. Sato and M. Sadatomi, Momentum and heat transfer in two-phase bubble flow, *Int. J. Multiphase Flow* **7**, 167–190 (1981).
20. A. Serizawa, I. Kataoka and I. Michiyoshi, Phase distribution in bubbly flow. In *Second Int. Workshop on Two-phase Flow Fundamentals*, Troy, New York (1987).